KLOE Note n.^{o} 175/02
May 17, 2002

The calibration of the space-time relations in the KLOE drift chamber

G. Cabibbo[a], P. de Simone[b], A. Ferrari[c],
E. Pasqualucci[a], L. Passalacqua[b], L. Pontecorvo[a], T. Spadaro[a]

a) *Dipartimento di Fisica, Università "La Sapienza" & Sezione INFN Roma I, Roma, Italy.*

b) *Laboratori Nazionali di Frascati dell'INFN, Frascati, Italy.*

c) *Dipartimento di Fisica, Università "Roma Tre" & Sezione INFN Roma III, Roma, Italy.*

Abstract

The method developed for the calibration of the space to time relations (s-t relations) for the KLOE drift chamber is presented. Due to the full stereo geometry used in the chamber, a set of different s-t relations has to be used, depending on the cell shape as well as on the azimuthal direction of the track. The s-t parametrizations needed to fully calibrate the drift chamber are described. The whole calibration procedure, which uses cosmic-ray events and has been implemented at the online level, is presented. Finally, the drift chamber performance studied with cosmic rays and physics events (Bhabha-scattering and $K_S \to \pi^+\pi^-$ events) is shown.

Contents

1 Introduction

The KLOE drift chamber [1, 2] must be able to track the charged particles with an accuracy of $\sigma_{r\phi} \sim 200\,\mu$m per measured point.
To minimize the multiple scattering of low momentum (between 50 and 300 MeV/c) particles, as well as the $K_L \to K_S$ regeneration, a helium-based gas mixture has been chosen: 90%He – 10% iC_4H_{10}. The resulting total radiation length is $\sim$900 m, including the contribution of the 52 240 sense field and guard wires. The drift velocity for this helium-based gas mixture is not saturated, so that the s-t relation is not linear.
To maximize the fiducial volume available for the detection of K_L charged decays (the decay length is $\lambda_L \simeq 340$ cm), the drift chamber has been built with a 2 m radius. The isotropic distribution of the K_L charged decay products suggested an uniform filling of the chamber, which has been achieved with an all-stereo wire configuration and drift cells "almost" square-shaped. The distribution of the K_L vertices is such that the first ionization clusters released by the K_L charged decay products can drift toward the wires along all of the possible directions, which depend on the azimuthal emission angle ϕ of the tracks. [1]. Moreover, the shape of the electric field of the drift cells entails a dependence of the s-t relations on the ϕ direction of the tracks.
In addition, because of the all-stereo geometry of the drift chamber, the distortion of the cell shape is a function of the azimuthal coordinate, of the radius, and of the z coordinate of each cell. The cell shape affects therefore the s-t relations, too.
All of the above reasons make the calibration of the KLOE drift chamber a peculiar and extremely delicate task.
In the following, we describe the drift chamber geometry, the parametrization of the s-t relations, and the calibration method which has been implemented. Finally, we present the performance of the online drift chamber calibration procedure.

2 The drift chamber geometry and the parametrization of s-t relations

The tracking detector of the KLOE experiment is a cylindrical drift chamber, with a diameter of 4.0 m and a length of 3.3 m, which is surrounded by a hermetic calorimeter. Both are immersed in a 0.52 T axial magnetic field. Both ends of the cylinder are closed by two spherical end-plates, with a radius of curvature of 9.76 m. The 12 582 single-sense-wire cells of the drift chamber are arranged in 58 circular layers. The cell area is of $\simeq 2\times 2$ cm^2 for the 12 innermost layers ("small" cells) and of $\simeq 3\times 3$ cm^2 for the outermost

[1] In all previous collider experiments, the charged tracks originate from the interaction point or close to it and cross radially the tracking volume. The drift direction of the ionization clusters is then roughly independent on the azimuthal direction of the tracks.

46 layers ("big" cells). The drift cells exhibit a ratio of field to sense wires of 3 : 1, for a total of 52 240 wires (including the two guard layers).
As already pointed out, the wires are in all-stereo configuration in order to have an uniform filling of the drift chamber. In order to measure the z coordinate of the tracks, the sense layers have a stereo angle Θ, which is opposite in sign layer by layer. As a consequence of this geometry, the distance of the wires of the k^{th} layer from the chamber axis varies continuously along z, reaching its maximum value at the end plates (R_k), and the minimum at the center of the chamber (R_{k0}). The difference $\delta = R_k - R_{k0}$ is kept constant for all layers in order to minimize the radial cell deformation along the longitudinal direction.
The relation between the stereo angle and the distance δ is:

$$\tan\Theta_k = \pm\frac{2\delta}{L_k}\sqrt{\frac{2R_{k0}}{\delta} - 1},$$

where L_k is the distance between the chamber end-plates for the wires of the k^{th} layer. The requirement of good resolution in the measurement of the z coordinate ($\sigma_z = \sigma_{r\phi}/\tan\Theta \simeq$ 2 mm), together with that of a reasonably small stereo angle, led to the choice of $\delta = 1.5$ cm. The stereo angle therefore increases with the radius, from $\simeq \pm 63$ mrad to $\simeq \pm 148$ mrad.
In this all-stereo configuration, the shape of the square drift cells changes along the z axis with a periodicity given by:

$$\Delta z = \frac{h/4}{|\sin(\Theta_k - \Theta_{k+1})|}$$

where h is the cell radial dimension. Because of the alternating stereo angles of the sense layers, a different periodicity is observed between the upper part ($\Delta z \sim 8$ cm) and the lower part of the cells ($\Delta z \sim$ twice the longitudinal dimension of the chamber).
Figure 1 shows the layout of the wires in one section of the chamber. To build a map of the wire arrangement inside the chamber, the cells have been classified on the basis of their shape using the angles β_1 and β_2 sketched in figure 2. Figure 3 shows the distributions of the two angles for cells at the plane $z = 0$. These distributions do not significantly change as a function of z.
Gas gain of $\sim 10^5$ and safe operation conditions in terms of aging in the DAΦNE radiation environment, with a helium-based gas mixture, are obtained with sense wires of 25 μm and field-shaping wires of 80 μm at a voltage difference of 1750–1900 V. With these choices, and a magnetic field of 0.52 T, we obtain the drift line configuration shown in figure 4 for small and big cells with $\beta_1 \simeq \beta_2 \simeq \pi/2$. The relevant properties of the gas mixture, either measured directly [3, 4, 5], or computed with transport equations [6, 7], are listed in table 1.
Starting from the results of the analysis on drift chamber prototypes [8], extensive simulation studies based on the `GARFIELD` simulation program [9] have been performed, in order to parametrize the cell response [10].

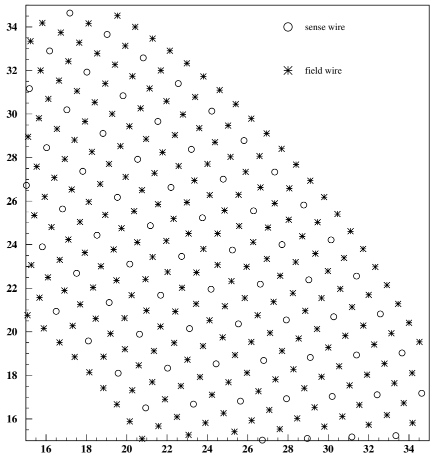

Figure 1: *Layout of the wires in one section of the KLOE drift chamber.*

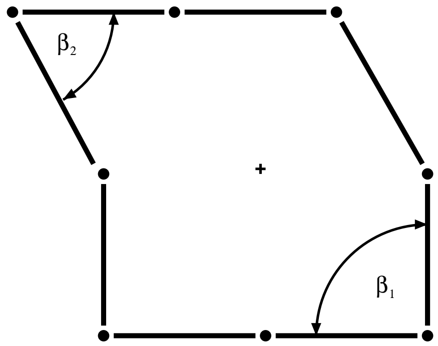

Figure 2: β_1 *and* β_2 *angles.*

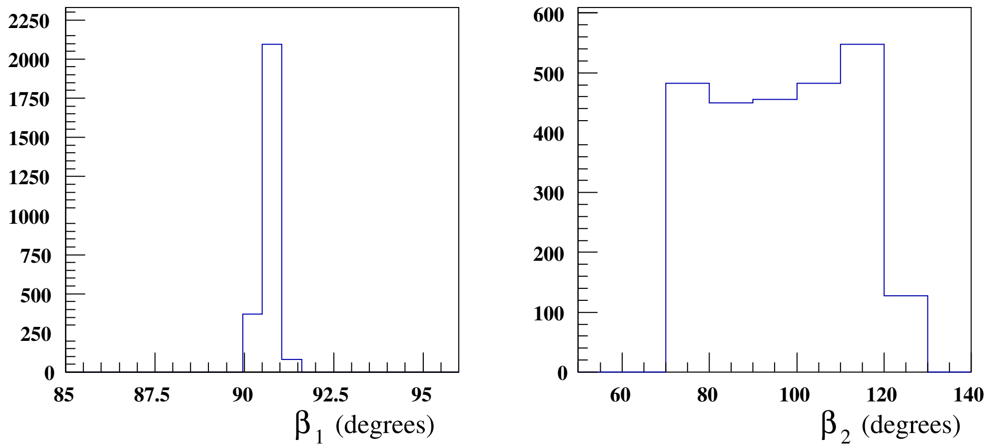

Figure 3: β_1 *and* β_2 *angle distributions in degrees at the plane* $z = 0$.

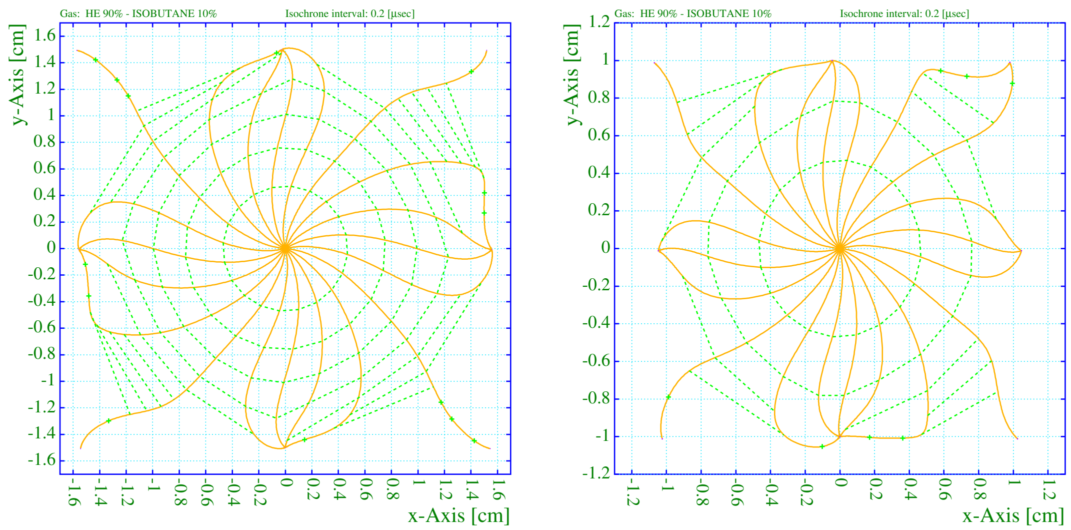

Figure 4: *Example of the drift lines for a big (left) and a small (right) cell.*

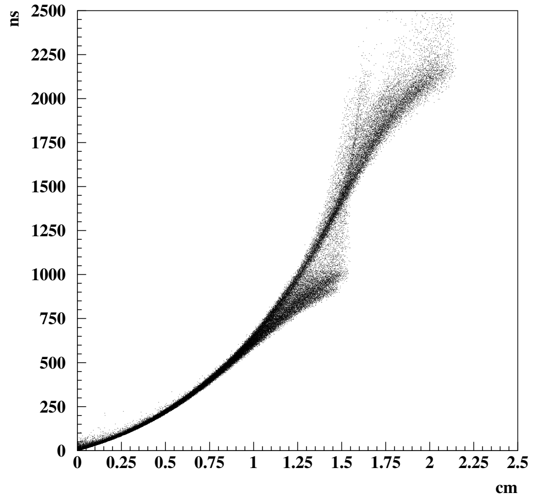

Figure 5: *Simulated s-t relation for cells with area* $3{\times}3\ cm^2$*, and shape defined by* $\beta_1 \simeq \beta_2 \simeq \pi/2$.

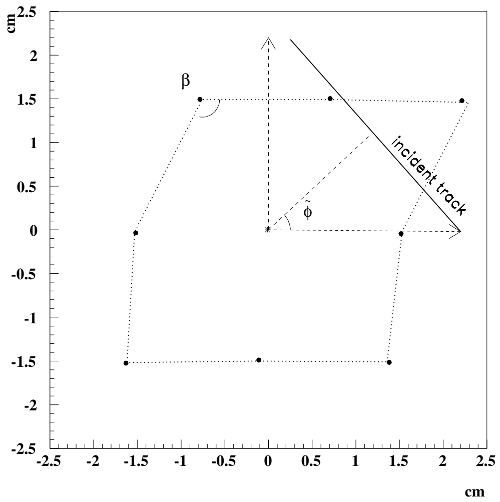

Figure 6: *The parameters used to classify the s-t relation's: the angles* β *and* $\tilde{\phi}$.

Parameter	Value	Reference
Number of primary clusters	$12.3 \pm 0.2\,\mathrm{cm}^{-1}$	[3, 4]
Total specific ionization	$\sim 9\,\mathrm{cm}^{-1}$	[4]
Drift velocity, $E = 0.5$–$1\,\mathrm{kV/cm}$	1.7–$2.3\,\mathrm{cm}/\mu\mathrm{s}$	[3]
Drift angle, $E = 0.5$–$1\,\mathrm{kV/cm}$	0.2–$0.3\,\mathrm{rad}$	[3, 6]
Diffusion coefficient, $E = 0.5$–$1\,\mathrm{kV/cm}$	$(2.5$–$3.2) \times 10^{-4}\,\mathrm{cm}^2/\mu\mathrm{s}$	[5]
Radiation length	$\sim 1300\,\mathrm{m}$	–

Table 1: Properties of the 90% He- 10% iC_4H_{10} gas mixture.

In figure 5 a simulated s-t relation is shown, corresponding to incident tracks having all possible azimuthal angles and crossing a cell with $\beta_1 \simeq \beta_2 \simeq \pi/2$. Figure 5 shows that the distortions of the electric field strongly affect the s-t relation at big impact parameters. In order to parametrize the cell response over the greatest possible extent of the collecting area, it is therefore necessary to correct for the azimuth ϕ of the incident tracks. Simulation studies have shown that the parametrization of the s-t relations can be done in terms of the dependence upon the angle $\tilde{\phi}$, which is the angle between the drift direction of closest ionization cluster and the x axis of the local reference frame of the cell, as shown in figure 6. Besides, 6 different topologies of the cell shape (chosen as "reference cells") are enough to have a realistic description of the s-t relations over the whole chamber volume. The "reference cells" have been selected on the basis of the β_2 angle (named β in the following). Finally, in each of these "reference cells" the s-t relations are parametrized in 36 $\tilde{\phi}$ bins, each 10° wide (this choice is a compromise between the need to have a good description of the s-t relations and that to have a limited number of parametrizations). These studies have found substantial confirmation in the experience done with the full length prototype 1 of the KLOE drift chamber [8].

To summarize, since the deformation affects only the upper part of the drift cells, there are a total of $16 \times 6 + 20 = 116$ parametrizations for the small cells and an additional 116 for the big cells.

The s-t relations are parametrized using Chebychev polynomials up to 5^{th} order [2], a complete set of orthonormal polynomials:

$$t_{\mathrm{drift}} = P_{\mathrm{cheb}}(d) = C_0 + R_1(d) + R_2(d) + R_3(d) + R_4(d) + R_5(d)$$

where t_{drift} is the measured drift time and d is the track impact parameter to the sense wire. The five R polynomials are:

$$R_1 = C_1\,(2\,a - 1)$$

[2] The linear and parabolic terms of the Chebychev polynimials are more stable than the higher order terms, reflecting in a realistic way the changing of the s-t relations as a function of the cell shape and track crossing angles.

$$
\begin{aligned}
R_2 &= C_2\,(8\,a^2 - 8\,a + 1)\\
R_3 &= C_3\,(32\,a^3 - 48\,a^2 + 18\,a - 1)\\
R_4 &= C_4\,(128\,a^4 - 256\,a^3 + 160\,a^2 - 32\,a + 1)\\
R_5 &= C_5\,(512\,a^5 - 1289\,a^4 + 1120\,a^3 - 400\,a^2 + 50\,a - 1),
\end{aligned}
$$

where $a \equiv d/d_{\rm max}$, and $d_{\rm max}$ is the limit within which the fit procedure is able to produce a good parametrization of the s-t relation. The coefficients C_i $(i\!=\!0,\ldots,5)$ are functions of the angles $\tilde{\phi}$ and β and are determined by the calibration procedure, as discussed in the following section.

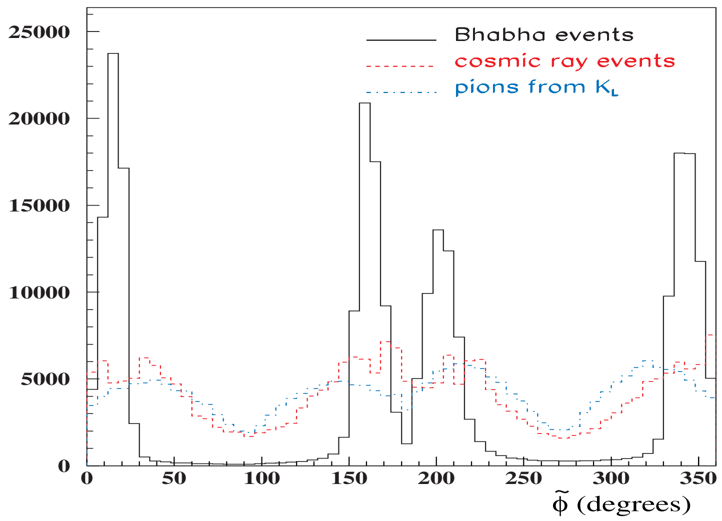

Figure 7: *$\tilde{\phi}$distributions for Bhabha tracks, pion tracks coming from the* CP*-violating events $K_L \to \pi^+\pi^-$, and cosmic-ray muon tracks.*

3 The calibration procedure

The calibration procedure aims at measuring and monitoring the s-t relations.

3.1 The selection of calibration events

Two kind of processes represent a natural choice to calibrate the s-t relations of the drift chamber cells: the e^+e^- pairs coming from Bhabha scattering and the cosmic rays.
Bhabha events are produced in large amount. Nevertheless, because the e^+e^- tracks originate from the interaction region and go through the drift chamber in radial directions, these events do not cover the entire range of $\tilde{\phi}$ populated by pions coming from K_L decays. This was the main motivation that led our choice to the cosmic-ray events as the main tool to calibrate the drift chamber. Figure 7 shows the comparison of the $\tilde{\phi}$ distributions for Bhabha tracks, pion tracks coming from the CP-violating events $K_L \to \pi^+\pi^-$, and cosmic-ray muon tracks.
The cosmic-ray events are selected online during the physics data taking by an algorithm [12] implemented in a level-3 filter, which partially reconstructs the raw events. These events are made available to remote analysis procedures via a KID [13] daemon. In section 3.5, the whole online procedure will be described.

3.2 Measurement of the cell t_0's

The time offsets for each of the 12 582 drift chamber channels are evaluated using cosmic-ray events selected with a dedicated trigger based on the information coming from the calorimeter.

We briefly summarize the different contributions to the time measurement. A first level trigger $T1$ is generated, under some conditions [15], $\sim$200 ns after the generation of each event. The signals coming from the sense wires are amplified and discriminated, and then give the *Start* to each TDC channel. Then, after a constant interval ($\sim 1.5\,\mu$s) which follows $T1$, a second level trigger $T2$ acts as the common *Stop* for all the chamber channels and gives the start to the acquisition system. $T1$ and $T2$ triggers are based on the topology of the energy deposit in the electromagnetic calorimeter, and/or on the number and the spatial distribution of the drift chamber hits [15]. The measured time t^i at the i^{th} cell is therefore:

$$t^i = T2 - t^i_{\text{Start}} = T2 - t^i_{\text{TOF}} - t^i_{\text{drift}} - t^i_{\text{wire}} - t^i_0$$

where t^i_{TOF} is the particle time of flight up to the closest primary ionization to the sense wire, t_{wire} is the propagation time of the signal along the wire, and t^i_0 is the offset due to the electronics chain from the preamplifier to the TDC input.

t_{TOF} and t_{wire} are computed without making use of any external tracker; information coming from the trigger and the calorimeter are used, and the cosmic-ray track is approximated with a straight line. Figure 8.a shows a typical distribution $t_{\text{drift}} + t_0$ for a single channel. This distribution is fitted with the function:

$$a + b \cdot \frac{e^{-d(t-t_1)}}{1 + e^{-(t-t_0)/c}}$$

The value of t_0 is computed as the inflection point of a Fermi-Dirac-like function, while the rest of the time distribution is described with an exponential. The noise is taken into account by the additional constant a and the parameter c is related to the time resolution close to the wire. Figure 8.b shows the stability of the above method, checked by comparing values of t_0 obtained with different runs, which were acquired under the same conditions (voltages and thresholds): the standard deviation is $\simeq$1 ns.
The offsets t^i_0's are calculated using cosmic-ray events at the beginning of each data taking period (few months), or whenever the experimental setting of the electronic chains was changed. The statistics required for the estimate of the t^i_0's is of $\sim 10^7$ cosmic-ray events.

3.3 The calibration method

The calibration program of the KLOE drift chamber is an iterative procedure which reconstructs tracks without making use of any external tracker, performs a quality check of the residuals (the difference between the impact parameters measured via the current parametrization and those given by the track fit), and, if required, produces a new set of calibration parameters.
As the trajectory of the particle is unknown at the level of the pattern recognition procedure, there are no information about the values of the $\tilde{\phi}$ and β parameters. The cell

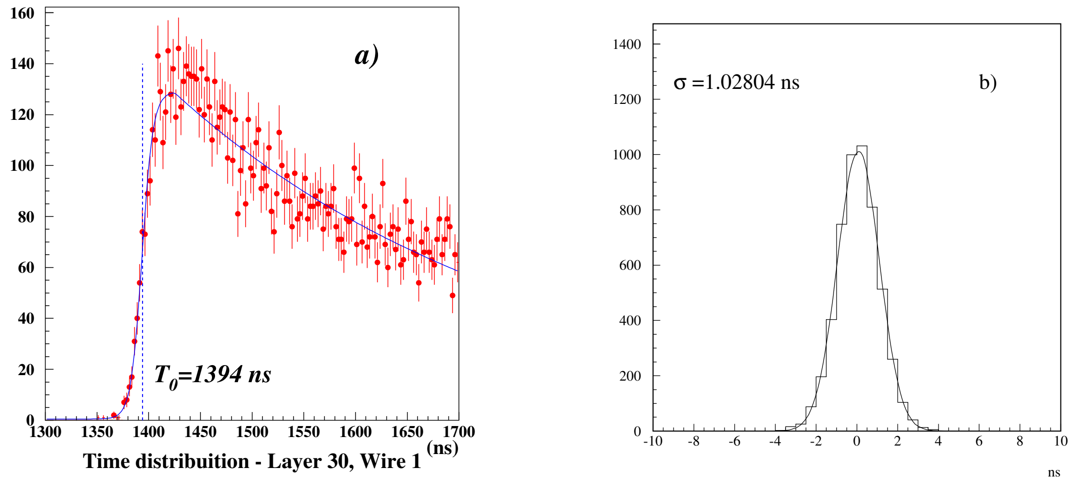

Figure 8: *a) Distribution of* $t_{\rm drift}+t_0$ *for a single wire. b) Stability of the* t_0 *estimates for a single chain.*

response is therefore described at this level by only one s-t relation, which is an average over all of the track orientations and drift cell shapes. This "raw" s-t relation is parametrized using three polynomials, each defined in a different space interval:

$$t_{\rm drift} = p_1(d) + p_2(d) + p_3(d),$$

where:

$$\begin{array}{rcll} p_1(d) & = & G_1 + G_2 d + G_3 d^2 + G_4 d^3 + G_5 d^4 & d \in [0.0, G_6] \\ p_2(d) & = & p_1(G_6) + p_1(G_6)' + G_7(d-G_6)^2 + G_8(d-G_6)^3 & d \in (G_6, G_9] \\ p_3(d) & = & p_2(G_9) + G_{10}(d-G_9) & d > G_9 \end{array}$$

The 10 coefficients G_j $(j=1,\ldots,10)$ include the connection points G_6 and G_9. In G_6, both the continuity and differentiability of the function are imposed, while in G_9 only the continuity is required. This function fits nicely the "raw" s-t relations of the small and big cells (see fig. 9).

Using this raw parametrization, the pattern recognition algorithm finds the track candidates for each event, allowing for an estimate of $\tilde{\phi}$ and β. Then, the track fit procedure computes the impact parameters d_n for each hit $(1,\ldots,n,\ldots,N)$ associated to each track candidate by inverting the appropriate Chebychev polynomial:

$$d_n = \left[P_{\rm cheb}(C_i^k, t_{\rm drift})\right]^{-1}$$

The 6×232 C_i^k coefficients ($k=1,\ldots,232$ and $i=0,\ldots,5$) define the "fine" s-t relations, which account for the cell type (small or big), the track orientation (the $\tilde{\phi}$ angle), and the

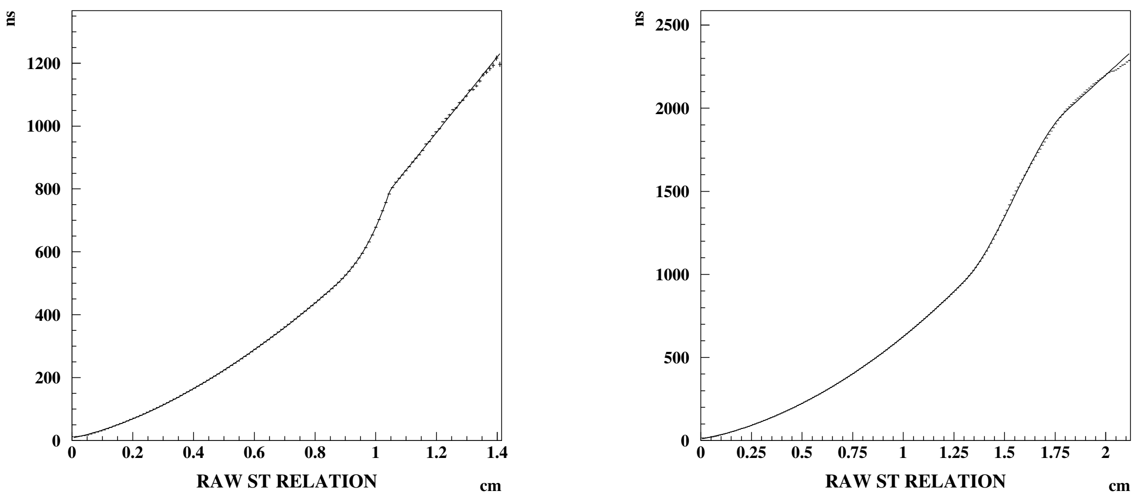

Figure 9: *Parametrization of the "raw" s-t relations for the* 2×2 *(left) and the* 3×3 *(right) cells.*

cell deformation parameter (the β angle). The input values of the G_j and C_i^k coefficients, as well as the resolution functions $\sigma(d)$ (see section 4.2), are set equal to the values calculated in the previous calibration run.
The residuals related to the "fine" and "raw" s-t relations are defined as $r_n^{\text{fine}} = d_n^{\text{fit}} - d_n(C_i^k, t_{\text{drift}})$ and $r_n^{\text{raw}} = d_n^{\text{fit}} - d_n(G_j, t_{\text{drift}})$. The distributions of residuals are binned in $300\,\mu$m-wide intervals of drift distance and are fitted with Gaussians to derive the mean values $\langle r_n^{\text{fine}} \rangle$ and $\langle r_n^{\text{raw}} \rangle$, and the variance in each bin. Using an iterative procedure (see section 3.4), the impact parameters d_n are corrected by minimizing the absolute values of the residuals for each parametrization. Then, the corrected values of d_n are used to perform a new reconstruction (pattern recognition and track fit procedures) of the tracks. The iteration is halted when for each of the 232 histograms the average (over the $300\,\mu$m-wide bins) of the residual distribution is smaller than $40\,\mu$m. As a final step, the 232 "fine" s-t relations (t_{drift} vs d_n^{fit}) are fitted, and the new sets of coefficients C_i^k are calculated.
In order to evaluate the threshold (mean residuals below $40\,\mu$m) above which an update of the calibration constants is required, we performed a Monte Carlo study using $K_L \to \pi^+\pi^-$ and $K_S \to \pi^+\pi^-$ events. We studied the changes in the track and vertex reconstruction efficiencies simulating different levels of miscalibration, corresponding to different average values $\langle \text{res} \rangle$ of the residuals distribution. As shown in table 2, the $K_L \to \pi^+\pi^-$ total reconstruction efficiency decreases by almost 1.7% passing from $\langle \text{res} \rangle \sim 10\,\mu$m to $\langle \text{res} \rangle \sim 50\,\mu$m. This is mostly due to the contribution of the K_L time of flight, which heavily affects the hit residuals of K_L tracks: a residual level $\langle \text{res} \rangle \sim 10\,\mu$m measured on the K_S tracks (or, equivalently, on the cosmic-ray tracks during the calibration) corresponds to $\langle \text{res} \rangle \sim 77\,\mu$m on the K_L tracks. For this reason, the $K_S \to \pi^+\pi^-$ reconstruction efficiency is much less sensitive, decreasing only by 0.3% under the same changes in the

residual levels.

	$K_L \to \pi^+\pi^-$				$K_S \to \pi^+\pi^-$			
$\langle\text{res}\rangle$ [μm]	$\varepsilon^2_{\text{pr}}$ [%]	$\varepsilon^2_{\text{trk}}$ [%]	ε_{ver} [%]	ε_{tot} [%]	$\varepsilon^2_{\text{pr}}$ [%]	$\varepsilon^2_{\text{trk}}$ [%]	ε_{ver} [%]	ε_{tot} [%]
10	90.96	96.06	88.69	77.50	96.50	99.45	96.39	92.50
30	90.54	96.21	87.64	76.61	96.31	99.51	96.45	92.43
50	90.75	95.93	87.45	76.15	96.33	99.36	96.28	92.15
70	90.75	95.84	87.02	75.68	96.42	99.39	96.19	92.19
90	90.58	96.22	85.74	74.74	96.42	99.44	96.11	92.14

Table 2: The Monte Carlo reconstruction efficiencies for pions of $K_L \to \pi^+\pi^-$ and $K_S \to \pi^+\pi^-$ decays are shown as a function of the mean value $\langle\text{res}\rangle$ of the residual distribution in the central part of each cell. The total efficiency ε_{tot} is written as a product of conditional probabilities: $\varepsilon^2_{\text{pr}}$ to have both π^+ and π^- pattern candidates, $\varepsilon^2_{\text{trk}}$ to have both reconstructed tracks, and ε_{ver} to reconstruct a vertex.

The dependence of the vertex spatial resolution for pions from $K_S \to \pi^+\pi^-$ and $K_L \to \pi^+\pi^-$ decays on the accuracy of the calibration of the s-t relations has also been studied. This dependence is negligible for reconstructed $K_S \to \pi^+\pi^-$ vertices, being the K_S vertices more affected by the uncertainty in the extrapolation of $\pi^\pm$ tracks beyond the drift chamber inner wall. On the contrary, the accuracy of the calibration is important for $K_L \to \pi^+\pi^-$ vertices, which are completely reconstructed within the tracking volume, as shown in table 3.

$\langle\text{res}\rangle$ [μm]	$\sigma_{\text{vtx}}(\hat{x})$ [μm]	$\sigma_{\text{vtx}}(\hat{y})$ [μm]	$\sigma_{\text{vtx}}(\hat{z})$ [mm]
10	400	400	1.3
30	470	450	1.35
50	500	450	1.45
70	550	500	1.5
90	550	600	1.6

Table 3: The Monte Carlo vertex resolutions for pions of $K_L \to \pi^+\pi^-$ decays are shown as a function of the mean value $\langle\text{res}\rangle$ of the residuals distribution in the central part of the cell.

In the next section, the complete calibration procedure is described in detail.

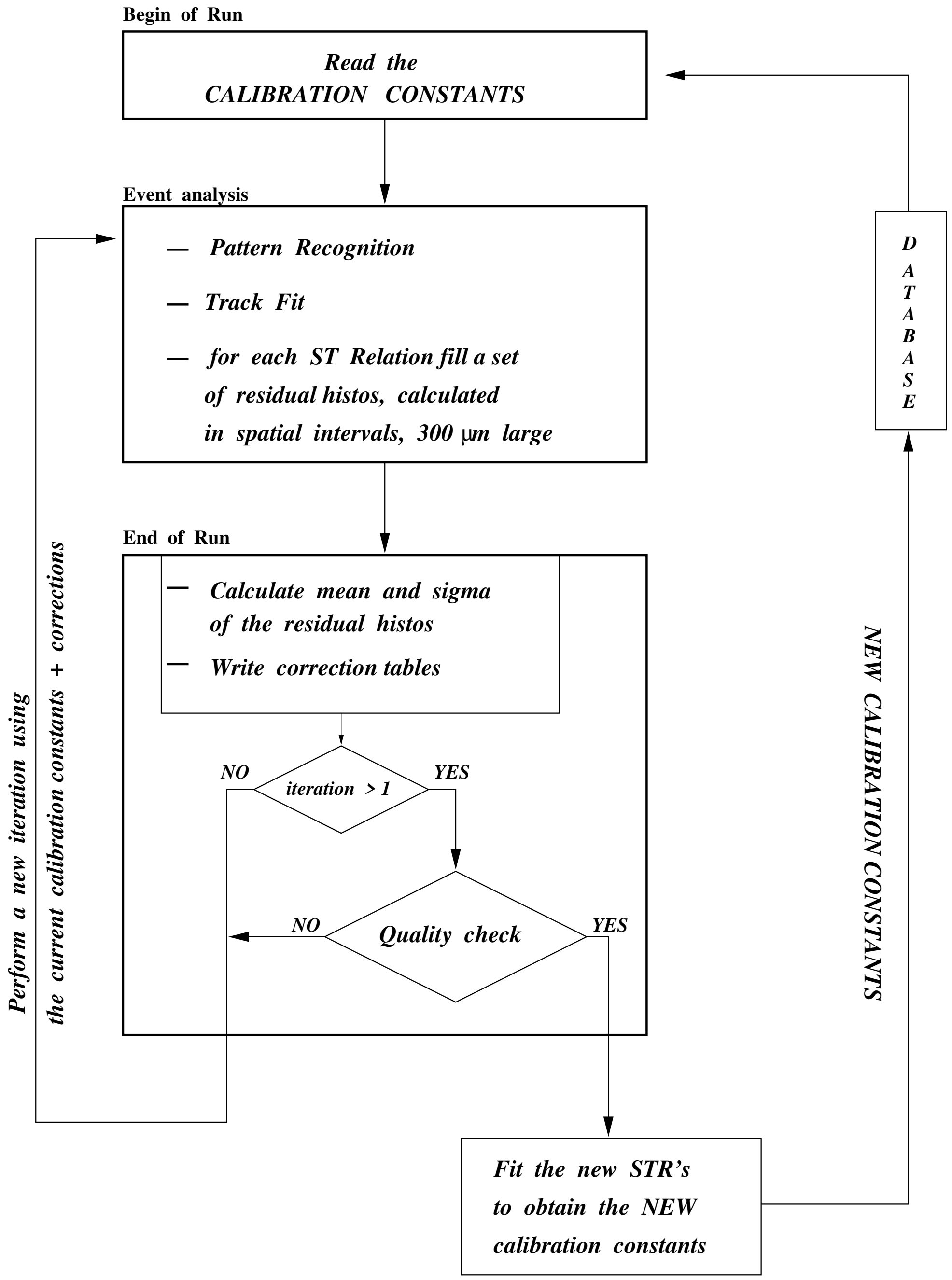

Figure 10: *Logical structure of the DCALIB calibration program.*

3.4 DCALIB: an AC module for the drift chamber calibration

3.4.1 The iterations with the 'correction tables'

A flow diagram of the program is shown in figure 10. For each generic $n^{\rm th}$ hit associated to a fitted track, the event analysis routine (`DCAEVT`) retrieves the following informations: $t_{\rm drift}$ from the `DTCE2` bank, $d_n^{\rm fit}$ from the `DHSP`, as well as the parameters $\tilde{\phi}$ and β, and the cell dimension. For each of the $2+232$ (raw+fine) s-t relation to be fitted, a set of residuals histograms are filled. Each histogram corresponds to a different interval of impact parameter $p=300\,\mu$m wide. The histograms span a range of impact parameter going from 0 to the half-width of the cell.
In the end-of-run routine (`DCARFI`), Gaussian fits to the previous histograms are performed. The mean values $\langle r\rangle^{(m)}$ and their errors $\delta r^{(m)}$ ($m=1,\ldots,$ last interval in d_n), are used to write a "correction table" in a YBOS bank, which will be used in the next iteration. The mean values of the residuals are added to the previous s-t relations at the center of each $300\,\mu$m-wide bin and a linear interpolation is used within these bins. In the generic iteration l, the corrected drift distance is:

$$d_n^{(l)}(C_i^k, t_{\rm drift}) = d_n^{(l-1)}(C_i^k, t_{\rm drift}) + {\rm corr}^{(l-1)}$$

where obviously $d_n^{(0)}$ comes from the current s-t relation and:

$$m=1 \rightarrow \qquad {\rm corr}^{(l)}(1) = {\rm corr}^{(l-1)}(1) + \langle r\rangle^1$$

$$m>1 \rightarrow \qquad {\rm corr}^{(l)}(m,d_n) = {\rm corr}^{(l-1)}(m,d_n) + \langle r\rangle^{(l-1)} + \frac{(\langle r\rangle^l - \langle r\rangle^{l-1})}{p}\cdot[d_n - p(m-\frac{3}{2})]$$

The procedure is iterated until the average of the corrections is smaller then 40 μm.
In figure 11, the distributions of the mean values of the residuals are shown as a function of the impact parameter of a single fine s-t relation ($\tilde{\phi}$=$360^\circ\pm5^\circ$) at the first (solid dots) and at the last iteration (open dots) of the calibration procedure, for a $2\times2\,{\rm cm}^2$ cell (top panel) and a $3\times3\,{\rm cm}^2$ cell (bottom panel). In this particular case, 2 iterations bring the residuals below $40\,\mu$m.

3.4.2 The s-t relation fit procedure and the new calibration constants

When the iterative procedure is completed, a new reconstruction of the sample is performed using the final correction tables, in order to fit the new s-t relations and to calculate the new Chebychev coefficients. $2+232$ new histograms of $t_{\rm drift}$ as a function of $d_n^{\rm fit}$ are produced. Each two-dimensional histogram is sliced in $110\,\mu$m-wide bins of d_n. Each slice is fitted with a Gaussian and the estimated mean values are used to plot the s-t relations. These are finally fit and the new constants are written into the database (HepDB).
In figure 12, a calibrated s-t relation corresponding to tracks with $\tilde{\phi}\sim 0^\circ$ is shown. The plot of the mean time values and the relative fit are superimposed. In figure 13, different typologies of calibrated s-t relations are shown.

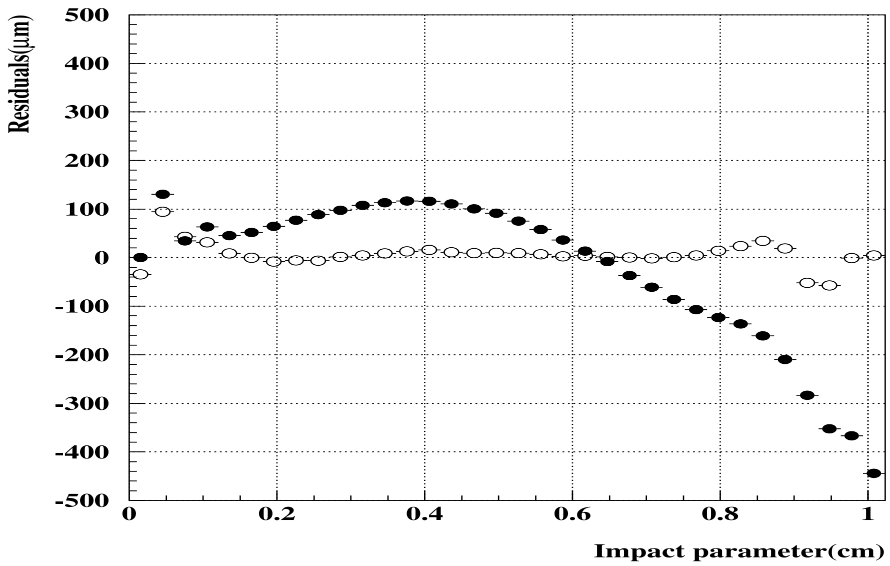

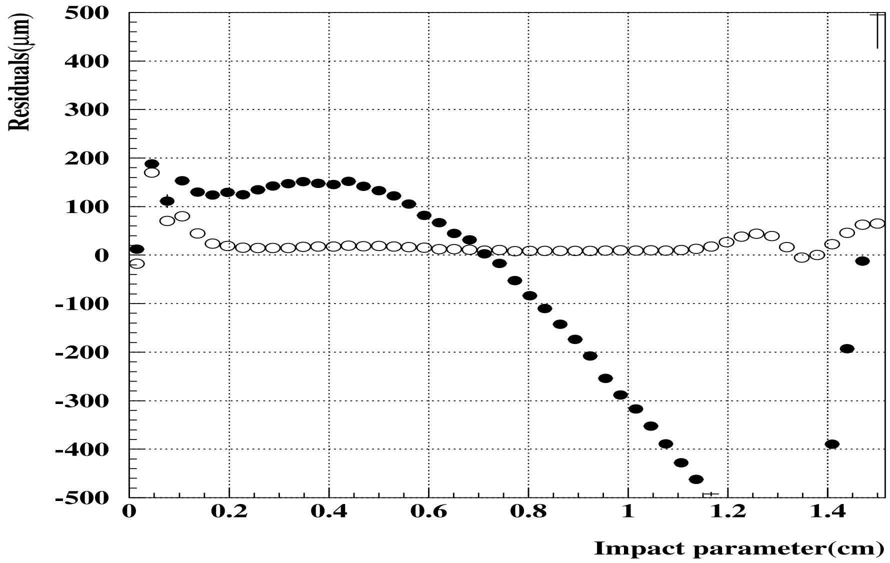

Figure 11: *Mean values of the residual distributions for the* $2 \times 2\,cm^2$ *(top) and* $3{\times}3\,cm^2$ *(bottom) cells, at the first (solid dots) and at the last (open dots) iteration of the calibration procedure.*

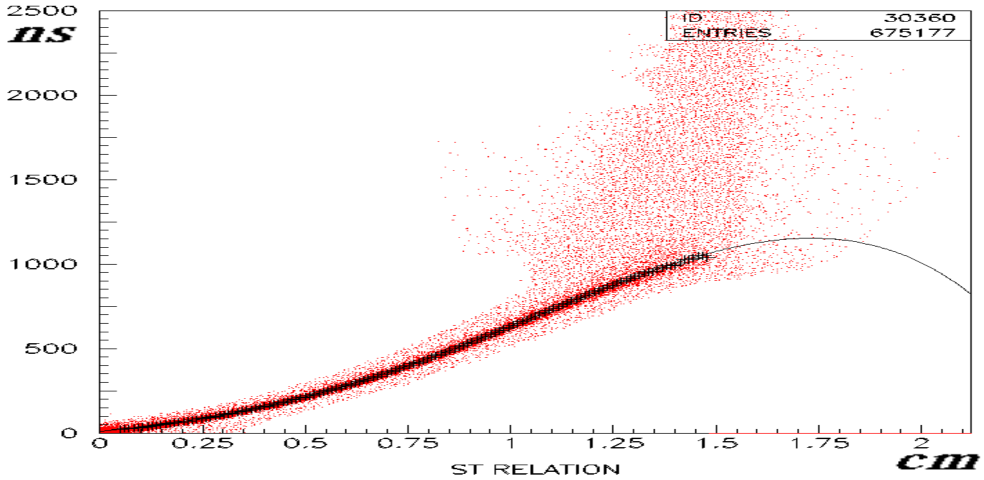

Figure 12: *The distribution of* t_{drift} *vs* d_n *for tracks with* $\tilde{\phi}\sim 0°$ *is shown, as calculated at the end of the last iteration with the correction tables. The plot of the mean values of the time distributions, calculated in narrow slices in* d_{drift}*, is superimposed and fitted.*

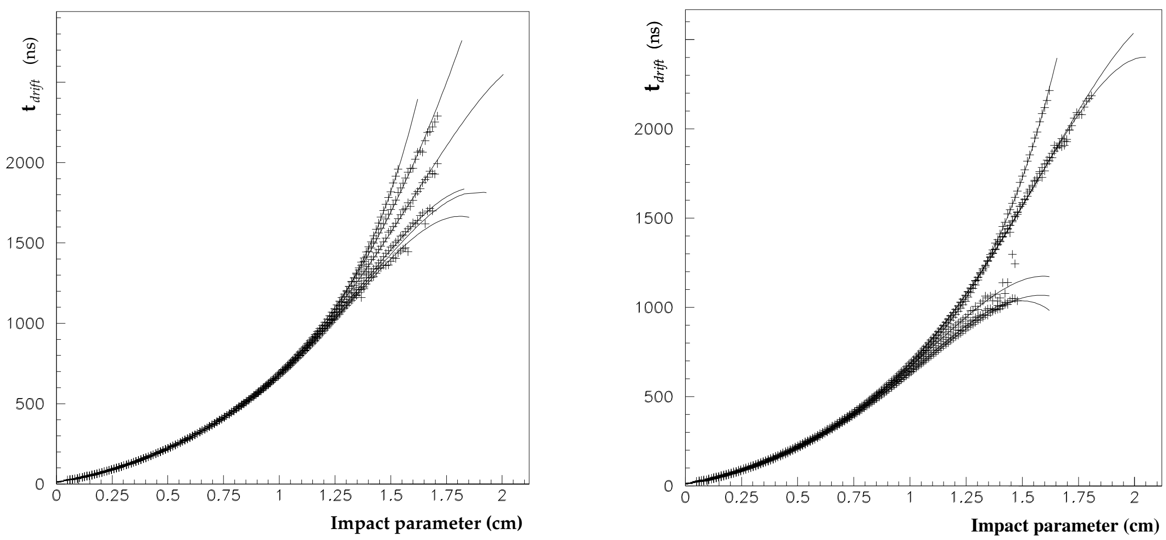

Figure 13: *s-t relations for different values of the angles* β *(left panel) and* $\tilde{\phi}$ *(right panel).*

3.5 The online monitoring of s-t relations

The calibration program described in the previous sections works in a more general online architecture, described in [14]. A schematic diagram of the DC calibration procedure is shown in figure 14. A synchronous procedure (`DC CHECK`) automatically starts at the beginning of each run. It takes selected cosmic events from all the event building nodes via the KID [13] mechanism and reconstructs them. Events with two reconstructed calorimeter clusters, one incoming and the other one outgoing, are then filtered (`DCTOF` stage), and the time of the incoming cluster is used to calculate the time of flight of the cosmic muon. These events are then tracked using the current parametrization of the s-t relations, and the absolute value of the average residuals is monitored in the central part of the cell, by using 80 000 events (`DC CHECK` stage). If the value exceeds $40\,\mu$m, 300 000 cosmic-ray events are collected and an asynchronous calibration program (`DC CALIB`) produces a new set of calibration constants.
Depending on the background conditions, the filters on the farm select events at a rate between 25 Hz and 30 Hz. The event collection takes therefore about $\sim$3 hours. Figure 15 shows the stability of various gas parameters during a typical period of data taking. All of the gas parameters are very stable, except for the atmospheric pressure, that can affect the reliability of the current parametrization of s-t relations.

4 Results and Drift Chamber performances

4.1 The spatial resolution

The resolution has been evaluated in each bin of reconstructed impact parameters [3] as the standard deviation of a Gaussian fit to the distribution of the residuals. Close to the sense wire, the quite low ionization density produces, besides of an increase of the average resolution, a systematic overestimation of the distance of closest approach. In these cases, this shift has been quadratically added to the RMS of the residual distribution in order to get a more realistic estimate of the total resolution. The figures 16.a and 16.b show the resolution averaged on all the "fine parametrizations", as a function of the reconstructed impact parameter. The spatial resolution is better than $200\,\mu$m over a large part of the cell, independently on the azimuthal direction of the tracks, and on the cell shape.

4.2 The resolution functions

The curves shown in figure 16 can be fitted with the quadratic sum of the main contributions to the spatial resolution [19]: the primary ionization statistics, the longitudinal electron diffusion, and the uncertainty in the drift time measurement due to the electronic

[3] The width of the spatial bins is of the order of the expected space resolution: $\simeq 200\,\mu$m.

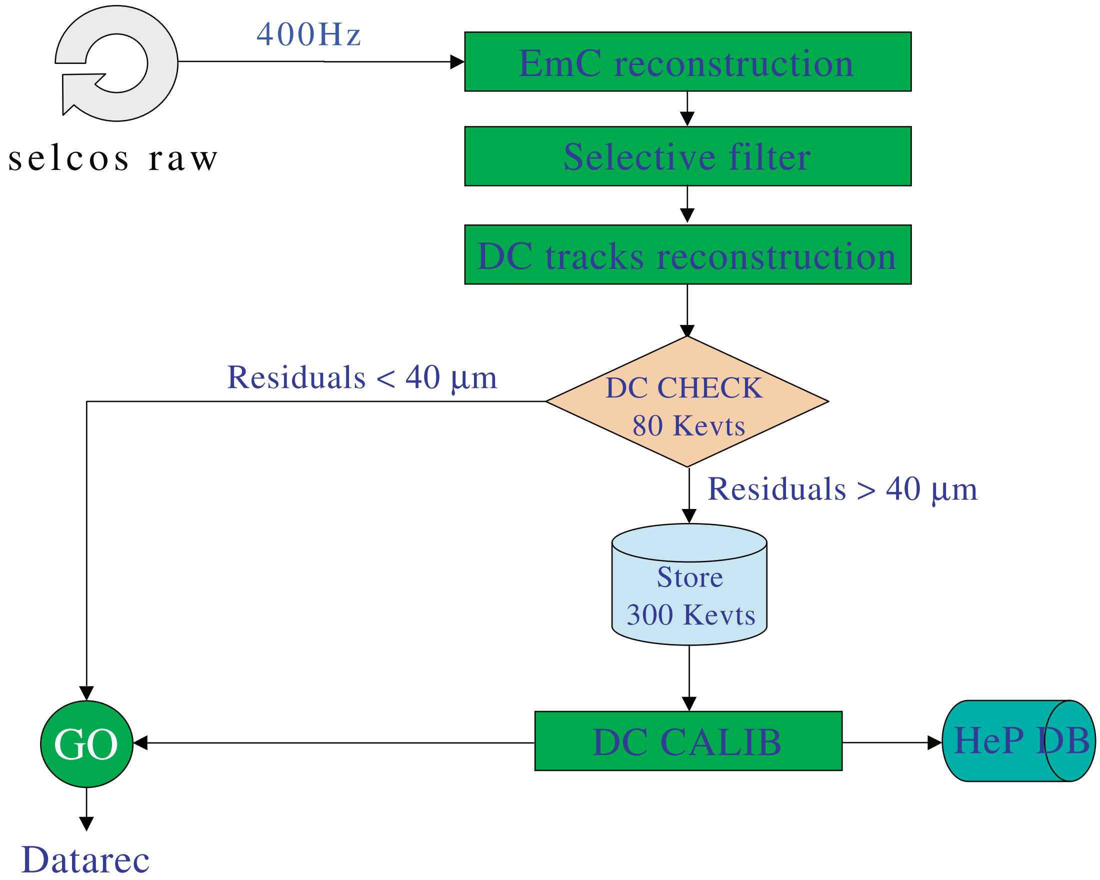

Figure 14: *Flow diagram of the online calibration procedure.*

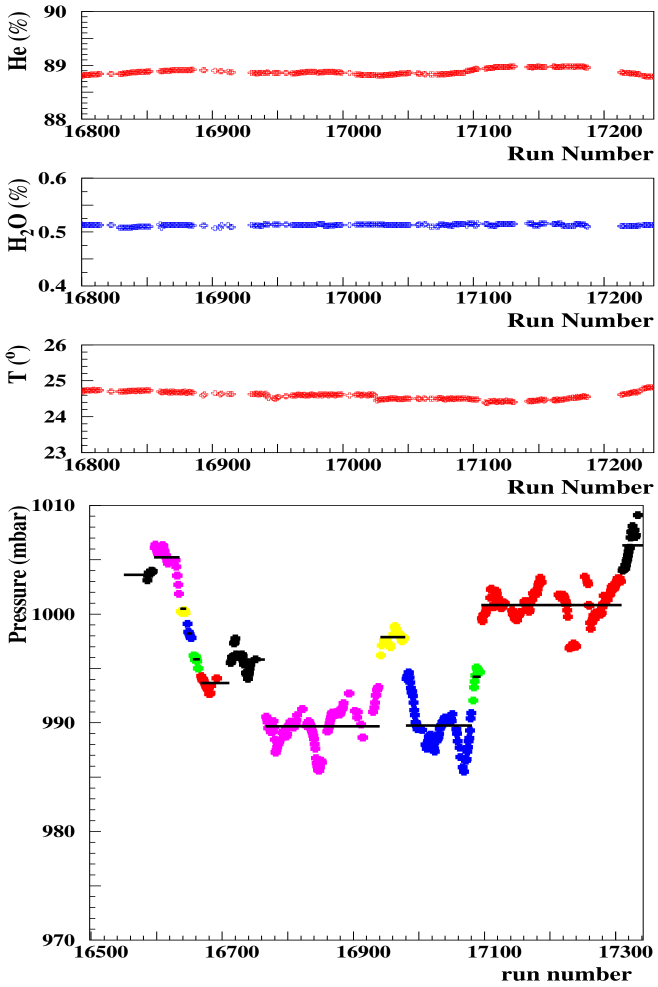

Figure 15: *Helium concentration, water vapour concentration, gas temperature, and gas pressure, as a function of the run number during the autumn 2000 data taking. A change in color in the pressure plot corresponds to an increased average of the residuals above* $40\,\mu m$*, so that a new calibration has been performed. The resulting s-t relations have been inserted in the database (HepDB), together with the average values of the pressure (black solid lines).*

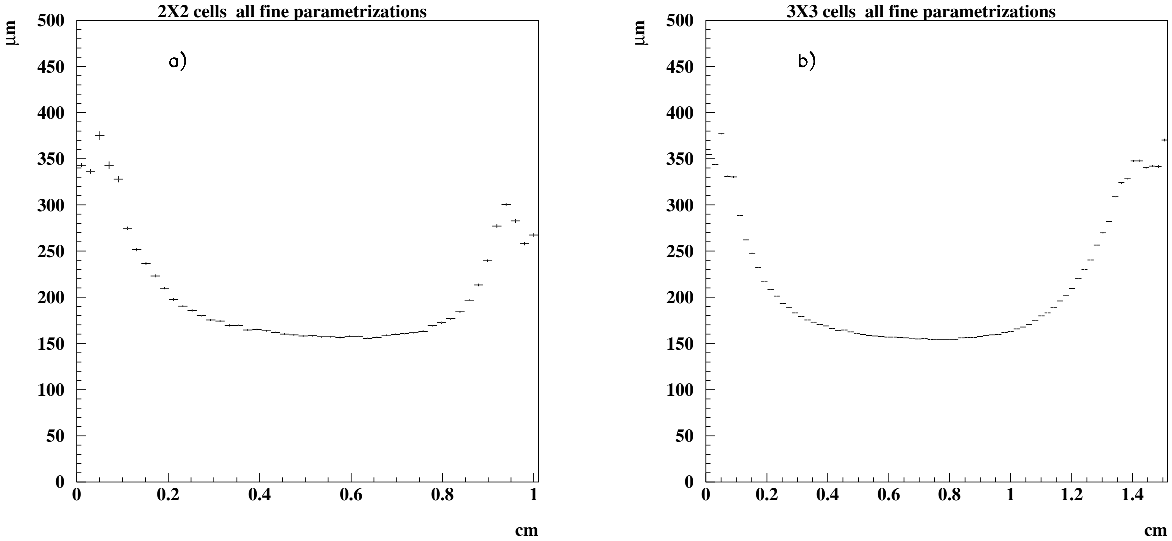

Figure 16: *a) Resolution as a function of the impact parameter for the* 2×2 cm^2 *cells. b) Resolution as a function of the impact parameter for the* 3×3 cm^2 *cells.*

noise. Figure 17 shows these fitted contributions. The range of impact parameter has been restricted to 1.1 cm only, in order to avoid as much as possible the area of the cell where the electric field is distorted due to the closeness of the field wires.

The primary ionization statistics has been parametrized as a function of λ, the mean free path between two consecutive ionizing collisions. The best fit gives $\lambda = (770 \pm 14)\,\mu$m, corresponding to $n_p = (12.9 \pm 0.1)$ clusters per cm for a minimum ionizing particle. This value is in very good agreement with those of Refs. [6, 20, 3].

The contribution due to the electron diffusion in the gas has been parametrized as the product of a term, which depends on the fraction f of the total ionization concurring to the arrival of the first electron, times the ratio of the diffusion coefficient $D(E)$ and the drift velocity $w(E)$ of the electrons in the gas [21]. The best fit to the distribution shown in figure 17 gives:

$$f = 10.24 \pm 1.67, \qquad \frac{D(E)}{w(E)} = (2.97 \pm 0.21) \times 10^{-4}\,\text{cm},$$

which implies a diffusive contribution of $\simeq 140\,\mu$m for 1 cm of drift. This number is comparable with the result of measurements of single-electron diffusion listed in Ref. [5]. The contribution due to the drift-time uncertainty is constant in the time domain, while is multiplied by the local drift velocity in the impact parameter domain. It is due to the time jitter of the electronics and the uncertainty in the knowledge of the t_0^i's. The fit to the curve of figure 17 gives $\sigma_t = (4.8 \pm 0.2)$ ns.

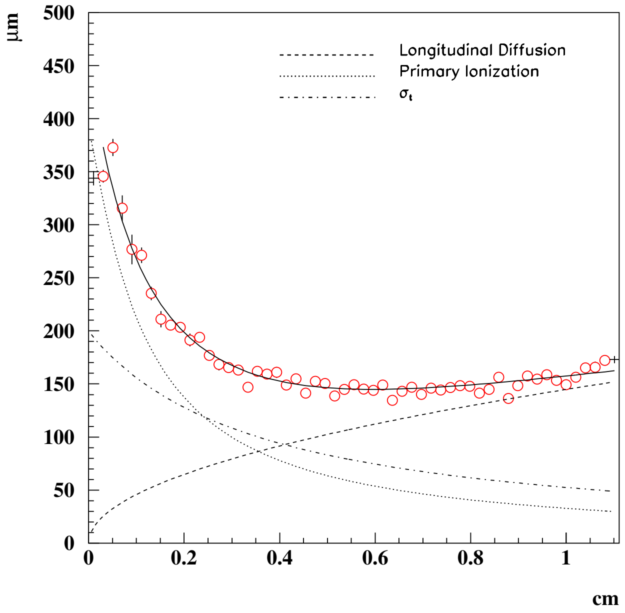

Figure 17: *Contributions to the spatial resolution coming from ionization statistics, longitudinal electron diffusion, drift time uncertainty.*

4.3 The quality of track and vertex reconstruction

In this section, some of the parameters related to the quality of the track and vertex reconstruction are shown. The momentum resolution for $e^{\pm}$ tracks in Bhabha events is plotted in figure 18. The relative resolution is about 2×10^{-3} for tracks with polar angle in the range $50° < \theta < 130°$.

The K_S invariant mass spectrum obtained using pion tracks of opposite charge coming from a vertex close to the interaction point is shown in figure 19. The spectrum has been fit around the peak with the sum of three Gaussians, giving a "principal" standard deviation of $\sim 800\,\mathrm{KeV}$.

It has to be stressed that the resolutions of these parameters are also affected by the accuracy in the knowledge of the magnetic field and by the tracking algorithm itself.

The tracking efficiency for pions produced in the $K_S \to \pi^+\pi^-$ decay has been measured on various data periods and has been compared with that observed in Monte Carlo [18]. It is practically independent on the polar angle θ of emission of the pion, except in the region $\theta < 30°$, where a significant decrease is observed (figure 20). Discrepancies between the plateau values for data and Monte Carlo (figure 21) can be ascribed to the presence in data of spurious hits in the innermost layers, due to machine background tracks of low p_t.

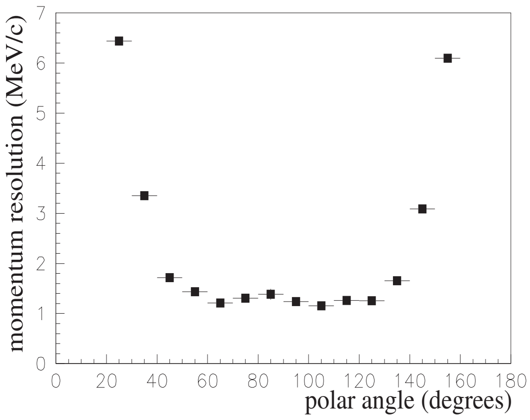

Figure 18: *The momentum resolution for* 510 *MeV electron and positron tracks from Bhabha scattering is shown as a function of the polar angle of emission.*

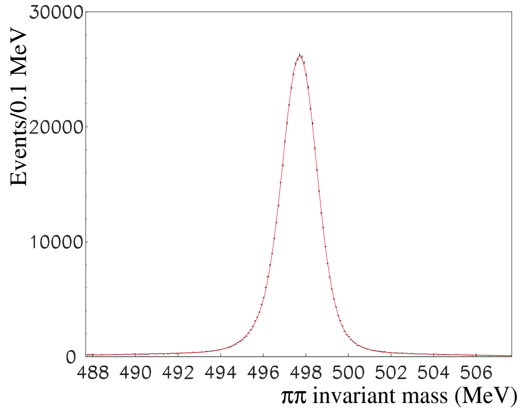

Figure 19: *Spectrum of the* K_S *invariant mass distribution obtained from a pair of oppositely charged tracks, coming from a vertex close to the interaction point.*

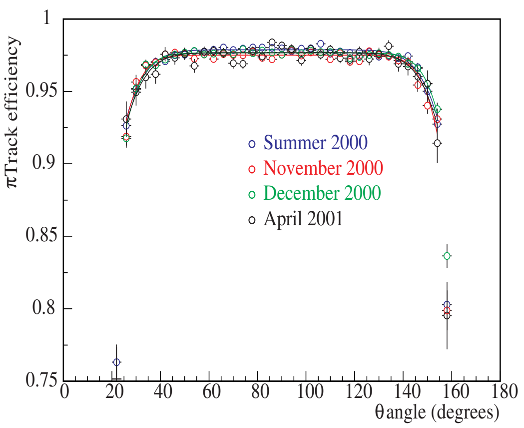

Figure 20: *The tracking efficiency for* K_S *pions is shown as a function of the polar angle of emission, for four periods of data taking.*

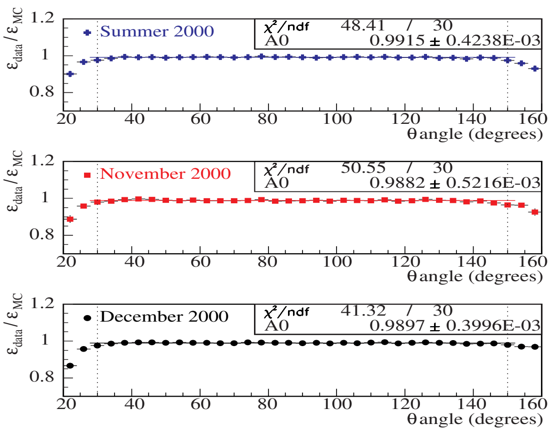

Figure 21: *The ratio between data and Monte Carlo tracking efficiency for* K_S *pions is shown as a function of the polar angle of emission, for three periods of the 2000 data taking.*

5 Conclusions

The complete procedure to calibrate and monitor the s-t relations of the KLOE drift chamber has been described. More then one year of running time shows that the method is robust and reliable, allowing us to monitor online any effect of variations of the external conditions on the s-t relations, and to give rapidly new sets of calibration constants. The spatial resolution largely satisfies the requirements of the experiment.

References

[1] The KLOE Collaboration, *The KLOE central drift chamber. Addendum to the KLOE technical proposal*, LNF-94-028 (June 1994).

[2] The KLOE Collaboration, *The Tracking Detector of the KLOE experiment*, preprint LNF-01/016(P), accepted on NIM A.

[3] C. Avanzini et al., Nucl. Instr. and Meth. **A 449**, 237 (2000).

[4] G. Bencivenni et al., *The prototype 0 of the KLOE tracking chamber*, KLOE Note **79**, (1993).

[5] V. Golovatyuk, F. Grancagnolo, M. Primavera, Nucl. Instr. and Meth. **A 394**, 97 (1997).

[6] A. Sharma and F. Sauli, Nucl. Instr. and Meth. **A 350**, 470 (1994).

[7] S. F. Biagi, Nucl. Instr. and Meth. **A 283**, 716 (1989).

[8] G. Finocchiaro, KLOE note no.92 (1994). R. de Sangro, KLOE note no.97 (1994). F. Lacava for the KLOE Drift Chamber group, Nucl. Phys. **B 54**, 327 (1997).

[9] *GARFIELD, a drift chamber simulation program*, CERN program library entry W5050.

[10] P. de Simone, KLOE note no.98 (1994).

[11] P. de Simone, *Studio di tecniche sperimentali per la ricostruzione del decadimento* $K_L \rightarrow \pi^+\pi^-$ *nell'esperimento KLOE a DAΦNE*, Ph. D. thesis (1994).

[12] The KLOE Collaboration, *NOVEL DAQ and Trigger Methods for the KLOE experiment*, hep-ex/0006039 (2000).

[13] The KLOE Collaboration, *KID - Kloe Integrated Dataflow*, Proceedings of CHEP'01, Beijing (2001).

[14] E. Pasqualucci, KLOE note, in preparation (2002).

[15] The KLOE Collaboration, *The KLOE trigger system*, Nucl. Instr. and Meth. **A 461**, 465 (2001).
M. Palutan, *CP violation studies at DAΦNE: the trigger of the KLOE experiment*, Ph. D. thesis (1999).

[16] A. Ferrari, *A measurement study of $K_L \to K_S$ regeneration cross sections at $p \sim 100$ MeV/c with the KLOE experiment*, Ph. D. thesis (1998).

[17] G. Cabibbo, *Misura di $\Gamma(K_S^0 \to \pi^+\pi^-)/\Gamma(K_L^0 \to \pi^0\pi^0)$ con il rivelatore KLOE* , Ph. D. thesis (1999).

[18] T. Spadaro, *Studies of K_S decays with the KLOE experiment*, Ph. D. thesis (2001).

[19] C. Luisi, KLOE memo no.78 (1997).

[20] G. Cataldi, F. Grancagnolo, and S. Spagnolo, Nucl. Instr. and Meth.**A 386**, 469 (1997).

[21] V. Palladino, B. Saudoulet, Nucl. Instr. and Meth. **128**, 323 (1975).